

Paper in press Acta Materialia 2009

PREDICTING GRAIN REFINEMENT BY COLD SEVERE PLASTIC DEFORMATION IN ALLOYS USING VOLUME AVERAGED DISLOCATION GENERATION

Marco J. Starink, Xiao Guang Qiao, Jiuwen Zhang, Nong Gao

Materials Research Group, School of Engineering Sciences, University of Southampton, Southampton
SO171BJ, UK

Abstract

The grain refinement during severe plastic deformation (SPD) is predicted using volume averaged amount of dislocations generated. The model incorporates a new expansion of a model for hardening in the parabolic hardening regime, in which the work hardening depends on the effective dislocation free path related to the presence of non shearable particles and solute-solute nearest neighbour interactions. These two mechanisms give rise to dislocation multiplication in the form of generation of geometrically necessary dislocations and dislocations induced by local bond energies. The model predicts the volume averaged amount of dislocations generated and considers that they distribute to create cell walls and move to existing cell walls/grain boundaries where they increase in the grain boundary misorientation. The model predicts grain sizes of Al alloys subjected to SPD over 2 orders of magnitude. The model correctly predicts the considerable influence of Mg content and content of non-shearable particles on the grain refinement during SPD.

Key words: Severe Plastic Deformation (SPD); equal channel angular pressing (ECAP); dislocation mobility; aluminium alloys; Grain size

1. Introduction

In most cases the main purpose of severe plastic deformation (SPD) processes such as equal channel angular pressing (ECAP, see Fig 1) [1,2,3] and high pressure torsion (HPT, see Fig. 2) [5,6,7] is to achieve a refined grain structure. Predicting the grain size attainable through SPD processes is important because the grain size will determine the strengthening achievable through grain boundary strengthening and because the grain size, especially that related to the stable high angle grain boundaries, has a major influence on superplastic forming properties [8,9]. These SPD processes are mostly conducted under cold deformation conditions, where dynamic recrystallisation is suppressed whilst strain rate dependence is very limited [1]. It is generally thought that FCC metals with grain size 50-100 nm deform predominantly via the slip of lattice dislocations, and for grains larger than 100nm they deform exclusively through this mechanism [10]. Various works have shown that in nanostructured materials (grain size < 50 nm) alternative deformation mechanisms involving

deformation twins [11,12,13], and stacking faults (SFs) [14,15] can occur. In some cases these types of defects have even been observed in grains with size up to 100 nm [12], but it is not evident that they make a significant contribution to deformation in these SPD processed materials.

Many researchers (see e.g. [16]) consider that the structure evolution during SDP processing broadly follows the classic mechanisms and concepts on structural changes occurring during conventional processes as shown in classic works [17,18,19,20,21]. At the early stage of deformation, a very high dislocation density is introduced, which leads to the formation of an intragranular structure consisting of cells with thick cell walls and low angles of misorientation. As the strain increases, the thickness of the cell walls decreases. These walls evolve into grain boundaries, and ultimately an array of ultra fine grains with high-angle non-equilibrium grain boundaries (GBs) [22,23,24] are formed. (Non-equilibrium grain boundaries may be present where there are non-geometrically necessary dislocations i.e. excess dislocations that do not contribute to the formation of misorientation at a grain boundary.) In broad terms we may term this the classic model for microstructure evolution in highly deformed metals. Xu et al. and Langdon [25,26] noted that the classic model would predict a gradually increasing refinement of the microstructure as a result of the continuous introduction of dislocation during the straining process. However, these researchers considered this to be inconsistent with some experimental observations and an alternative model based on an inter-relationship between the formation of subgrain boundaries and shear deformation during ECAP was proposed [25]. The model incorporates the geometries relevant to repeated ECAP passes (see Fig 1). The original grains become elongated to a band shape subgrain when the billet passes the corner in the first pass. In the second pass, the elongated subgrain is either further elongated (route C) because the shear plane remains in the same direction or sheared (route A and B_C) because the shear plane is changed to another direction. Especially when route B_C is used, several intersecting slip systems lead to a high density of dislocations and then these dislocations re-arrange and become subsumed in the grain boundary (some researchers consider the latter ‘annihilation’ of dislocations, as will become clear below we prefer to avoid that term). As a result, for route B_C, a reasonably equiaxed array of grains is formed.

Cell wall and grain boundary evolution involves various complex processes, see for instance [27,28]. Cell wall formation of low angle boundaries by dynamic recovery during the deformation. Low misorientation (1°) boundaries form a 3-d or 2-d cell structure which tends to remain equiaxed during deformation and are sometimes referred to as “incidental dislocation boundaries” [28]. Subgrain size tends to be constant at larger strains, and this is interpreted in terms of a dynamic equilibrium between dislocation generation and annihilation. But also other types of low angle boundaries have been identified. High angle boundaries can form by deformation banding in which grains may split on a coarse scale into several sections which then follow different orientation paths during subsequent deformation, or by increase in misorientation of the persistent boundaries discussed above. However, high angle boundaries may also evolve from low angle boundaries by assimilation of dislocations.

Further rigid body rotation during deformation of high angle boundaries, will tend to align them with the rolling plane, thus forming a lamellar microstructure [29].

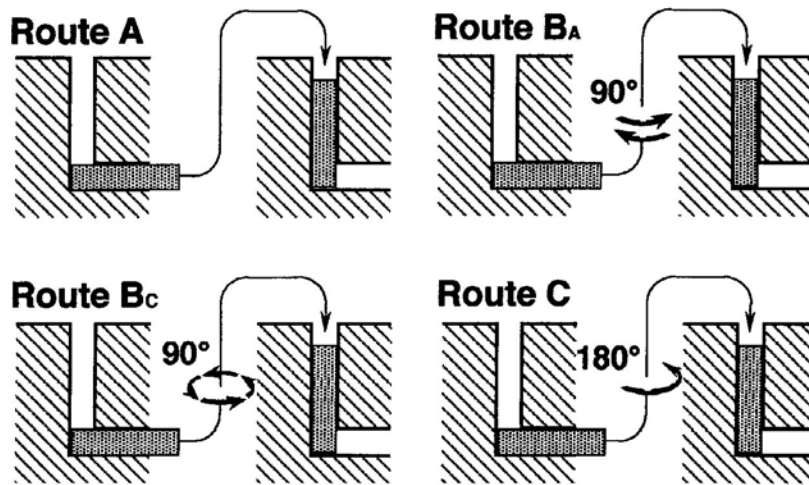


Fig. 1 Schematic illustration showing the billet and ECAP die, with the billet rotations during subsequent passes for the 4 basic routes of ECAP. (from [4])

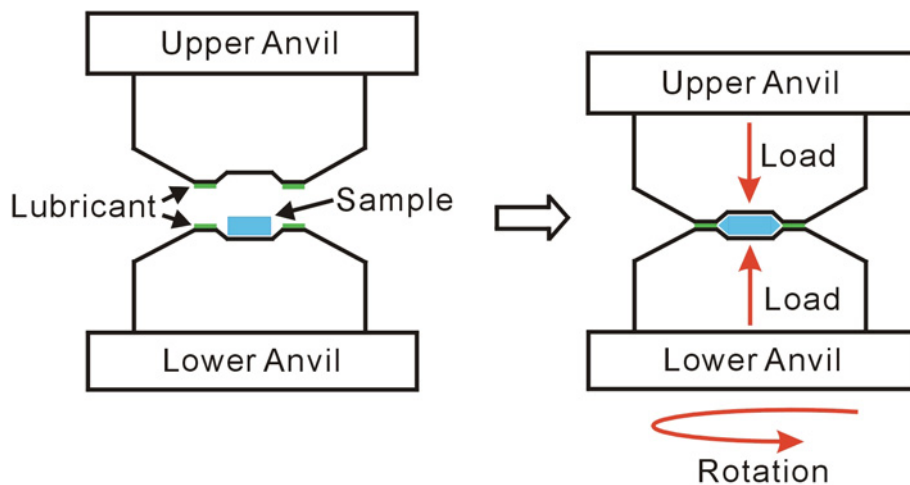


Fig. 2 The principle of high pressure torsion (HPT) (from [7])

Grain refinement during SPD is significantly influenced by the presence of non-shearable particles in the alloy, which can produce a factor 2 difference in grain size between alloys with different content of non-shearable particles [30]. Also elements dissolved in the matrix phase have a significant influence on grains refinement, with 3wt%Mg additions to Al causing about a factor 3 reduction in grains size. A model that quantitatively explains these effects has as yet not been available. It has been noted

(Beyerlein et al [31] and Signorelli et al [32]) that prediction of grain size evolution is principle possible in a visco-plastic self-consistent (VPSC) polycrystal model when combined with an (empirical) criterion for the grain subdivision process during ECAP. However, no reports on successful predictions of grain sizes have as yet appeared.

The aim of the present work is to derive a model for grain size in the SPD regime incorporating especially the effect of non-shearable particles and dissolved alloying elements. Our new model will employ some of the concepts from the models and papers reviewed above. However, to make the problem tractable, we will use a substantial simplification by treating only averaged dislocation densities as caused by averaged particle spacings and averaged solute contents, effectively reducing a 3D problem to volume averaged properties. This will effectively by-pass much of the details of the cell wall and boundary evolution processes in favour of a model describing a volume averaged behaviour. The model will be tested against microstructure data of several SPD processed Al based alloys. It proved possible to construct a simplified model with good predictive properties in closed form solutions, and hence we will provide a computationally efficient model.

The structure of the present paper is as follows. We will first introduce the materials, processing and experimental techniques applied in the work. Next we will present a model for grain size evolution illustrating several aspects of it with selected results from transmission electron microscopy (TEM) and electron backscatter diffraction (EBSD) work performed. Finally we will present a full description of results and a literature survey on published data for a critical comparison of model predictions with data.

2. Experimental: materials, processing and microstructure analysis.

Microstructure development during severe plastic deformation of 6 alloys was analysed; the compositions of these alloys are given in Table 1. Prior to SPD the Al-7034 and Al-1050 alloys had been extruded into a rod. (Note there are two batches of Al-1050 with slight differences in composition.) The Al-2024 alloy was cast, hot rolled to plate and subsequently heat treated to T3 condition. The Al-3Mg-0.2Mn was cast, hot rolled, solution treated and subsequently cold rolled. The other alloys were not thermomechanically processed prior to SPD, they were in as-cast and homogenized condition. The average grain size was 2.1 μm for the 7034 alloy and 45 μm for the 1050 alloy. The grain size for the Al-Zr and Al-Zr-Si-Fe alloys was very large, about 690 μm and 540 μm respectively. The grains in the rolled Al-2024 alloy were pancake shaped with sizes about 100 by 500 μm . The content of second phase particles is very different between these alloys. The 7034 has the highest amount of second phase particles by virtue of the high content of η phase particles present [33]. The amount of second phase particles is intermediate for the 1050 alloy, with the Al-Zr alloy having a very low amount of second phase particles.

Five alloys were processed by ECAP and 2 were processed by HPT (see Table 1). ECAP was conducted using a solid die with 9.7 mm diameter channel, with a 90° channel intersection angle (Φ) and a 20° curvature on the outer side of channel intersection (Ψ) (see Fig. 3). Specimens were lubricated with a suspension of MoS_2 in mineral oil ('ASO oil' supplied by Rocol) in order to reduce the friction between the plunger, specimen and the die. A careful alignment of the plunger and upper channel of the die was carried out. A plunger pushing speed of 0.5 mm/s was employed. After one pass of ECAP, another specimen was put in the die to push out the first specimen. Processing of Al-7034 and Al-2024 and selected microstructure analysis results on these alloys was reported before [33,34,35]. All SPD processing was carried out at room temperature, with the exception of ECAP on the Al-7034 alloy which was carried out at 200°C .

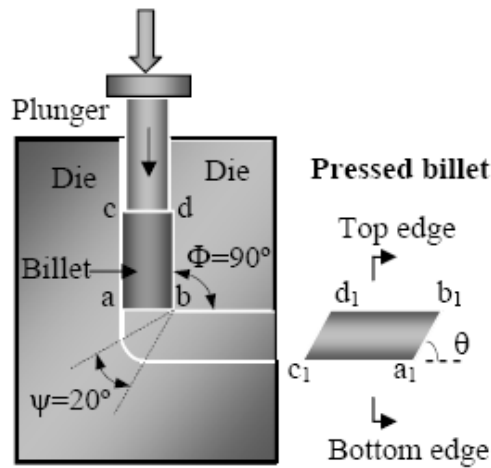


Fig. 3 Schematic illustration of the ECAP die.

Alloy	Composition [wt%]							grain size [μm] before SPD	SPD	
	Zn	Mg	Cu	Zr	Si	Fe	Mn		ECAP	HPT
Al-7034	11.5	2.5	0.9	0.2	-	-	-	2.1	✓	-
Al-1050 A	0.006	0.01	0.009	-	0.12	0.18	0.007	45	✓	-
Al-1050 B	0.006	0	0.008	-	0.14	0.26	0.005	45	-	✓
Al-2024	-	1.4	4.4	-	0.1	0.1	0.4	~200	✓	✓
Al-Zr	<0.01	<0.01	<0.01	0.15	<0.01	<0.01	-	690	✓	-
Al-Zr-Si-Fe	0.01	<0.01	<0.01	0.16	0.17	0.19	-	540	✓	-
Al-3Mg-0.2Mn	0.003	2.95	-	-	0.15	0.20	0.24	30×100	-	✓

Table 1: Compositions and grain size for the alloys studied subjected to SPD, with process that the alloys were subjected to.

Processing by HPT was conducted using disks having diameters of 10 mm and thicknesses of 0.9 mm. All processing by HPT was conducted at room temperature under pressures of 34.0 GPa and with torsional straining between 1 and 5 turns. No lubrication was applied on the sample. In additional tests slippage was found to be negligible.

Electron backscattered diffraction (EBSD) was used to characterize the microstructure as well as grain and subgrain boundary misorientation distribution in billets of all ECAP-processed alloys. Samples of 10 mm length used for EBSD analysis were machined from the middle of ECAP-processed billets. For sample preparation, the surface of cross section was first mechanically ground up to 4000-grit SiC paper, then electropolished employing an electrolyte composed of 33 vol% nitric acid and 67 vol% methanol. The electropolishing was carried out with a DC voltage of 20-30 V for 30 seconds. The electrolyte was cooled to and maintained at a temperature of -30°C using liquid nitrogen. The equipment used was a JEOL JSM6500F thermal field emission gun scanning electron microscope (FEG-SEM) equipped with an HKL EBSD detector and HKL Channel 5 software. The SEM accelerating voltage was set to 15 kV. Step size is reported with the results; in most cases it was between 0.1 and 0.5 μm . Orientation imaging microscopy (OIM) maps were obtained from the cross section perpendicular to the longitudinal direction of ECAP-processed billets. Intercept lengths were determined using an automated procedure. For misorientation angle distributions the lowest cut off angle was set at 2°.

TEM was conducted on Al-1050 subjected to ECAP and HPT, the Al-Zr alloy subjected to ECAP, and the 2024 alloy subjected to HPT. For TEM disks of 3mm in diameter were punched out from slices cut from the processed billets, ground to about 0.20 mm in thickness and then electropolished using a solution of HNO₃ and methanol (1:3 in volume). TEM foils were examined using a JEOL 3010 microscope operating at 300 kV.

EBSD analysis of grain size of an HPT processed (5 turns) Al-1Mg-0.3Mn alloy proved unreliable due to very low pattern identification rates, and it was decided to not use EBSD for HPT processed alloys. Instead, to supplement the TEM work on HPT processed samples, the grain size of selected HPT processed samples of an Al-1050 and Al-3Mg-0.3Mn alloys were studied through SEM. For this analysis samples were sectioned, ground and polished, and subsequently etched in Keller's reagent for 3 min to reveal grain boundaries. SEM was conducted on a JEOL JSM6500F FEG-SEM in secondary electron mode.

Grain sizes reported and quoted in this paper were determined through analysis of TEM, EBSD and SEM data. For EBSD analysis of grain sizes on our SPD processed alloys grain boundary intercept lengths, \bar{L} , were determined using an automated procedure, with lower cut off angle set at 2°. For reliable TEM grain size measurements it needs to be considered that not all grain boundaries in a sample will show a detectable contrast, and also finite sample thickness (causing overlap of grains in

the TEM image) needs to be taken into account. For TEM micrographs obtained for the alloys investigated by us and most TEM micrographs published in the literature, grain size was determined by us by considering only the 20-30% of the micrograph with the lowest beam intensity (i.e. darkest grains) and subsequently eliminating all areas with aspect apparent aspect ratio larger than 2 (because these are likely to be due to overlapping grains). Subsequently intercept lengths were determined on random lines. A correction was made for TEM foil thickness, which is assumed to be $120\pm 50\text{nm}$. (Note that much of the literature in the field does not seem to consider this correction.) When this procedure produced less than 5 grains, we included more grains up to at least 5 grains were included. In selected other cases grain size data used in this work was obtained directly from grain sizes reported in published work (e.g. Ref [36]). We will report accuracies of determinations of average grain size which take into account the uncertainty concerning foil thickness and distribution of sizes. For analysis of SEM micrographs of etched samples, a line intercept method was used. Care was taken to avoid areas where overetching was obscuring grain boundaries. There is a range of ways in which an ‘average’ grain size can be defined (see e.g. [37]). Although sometimes \bar{L} has been taken as ‘grain size’ it is actually an underestimate of most realistic definitions of the grain size, and in this paper we will report the grain size, d , consistently as $d = 1.455 \bar{L}$. This is based on $d = \bar{V}^{1/3}$, \bar{V} being the average cell volume, with the assumption of a Poisson-Voronoi size/shape distribution (see Section 3.3). Accuracy of experimental d determinations is typically $\pm 8\%$ (1 standard deviation), rising to $\pm 15\%$ for cases where less than 10 grains can be reliably detected.

To elucidate elements of the model, tensile tests were performed on 15 further alloys. The compositions of these alloys are given in Table 2 (alloys marked ‘this work’). The first 9 low Cu Al-Mg-(Cu)-Mn alloys were direct chill (DC) cast, the cast ingots were preheated and homogenised at 540°C , and subsequently hot rolled down to 5 mm in thickness. After that, the hot rolled and cold rolled to required reduction, and subsequently solution treated at 500°C . The Al-Cu-Mg and Al-Li-Cu-Mg alloys were produced by conventional casting followed by hot rolling. They were all solution treated at 495°C . The tensile testing was conducted according to the ASTM-E8M standard. The tensile axis is taken in the longitudinal (L) direction (i.e. the rolling direction). For each condition usually two tests were performed. Tensile tests were performed using an 8800 series Instron machine at a constant strain rate of 0.001 s^{-1} . Selected processing and microstructure data on the Al-Mg-(Cu)-Mn, Al-Cu-Mg and Al-Li-Cu-Mg alloys was reported before [38,39,40]. From the tensile test data K_A (as defined in Section 3.2) was determined from the flow stress between 0.01 and 0.05 plastic strain. Accuracy of experimental K_A determinations is typically $\pm 15\text{MPa}$, or 4%, whichever is the greater.

3. The model and supporting microstructural data.

3.1 General model structure and main assumptions.

Most available models on grain refinement during SPD follow the strategy of considering the gradual evolution of the microstructure starting from low strains up to the very high strains typical of SPD [28, 31,41,42,43]. An important factor in these models is the details of cell wall and subgrain boundary formation. Whilst recognising the value of those models, especially in elucidating the processes occurring at low and medium strains in 3D, we note that these approaches have not led to a model that is successful in predicting grain sizes of alloys subjected to SPD. In this work will depart from this approach and aim to produce a model that predicts grain sizes in the regime of SPD (effective strains in excess of 3). The model does not include any qualitative predictions on cell and subgrain formation, we just acknowledge that it does occur and is dominant at low to medium strains. We will introduce a substantial simplification in treating only averaged dislocation densities as caused by averaged particle spacings and averaged solute contents, effectively reducing the 3D dislocation movement and cell wall creation case to a volume averaged model. As a consequence the spatial pattern of the grain boundaries has no direct relation to the spatial arrangement of particles and the original orientation of the crystal lattice. We will thus limit ourselves in this work to considering SPD processing routes that lead to grain structures that are close to being equiaxed.

Within the model we view a dislocation as being the border of a surface where slip has occurred. It is the cumulative effect of this deformation on a range of slipped surfaces that determines changes in the CW/GB misorientation angle. When a dislocation is assimilated in a CW/GB it may appear ‘annihilated’ in the sense that it can not be discerned in TEM, but in the sense of being the border of a 2D surface where slip has occurred it has not disappeared: it is present in the grain boundary at the intersection of the slipped surface and the grain boundary. (These views are in many ways comparable and compatible to the more elaborate treatments by Estrin, Toth and co-workers [41,43] which incorporates low angle grain boundaries / cell walls of finite thickness and a finite volume density of dislocations. In terms of the concepts these latter works, we are here considering an infinitely thin grain boundary, and an area density of dislocations; and we expand that treatment by extending it to higher angle grain boundaries.)

We will show that the grain size can be predicted well by considering the total amount of dislocations formed in the straining process, without regard to the detailed geometry and mechanisms of cell wall formation. To simplify terminology we will term any feature that is either a cell wall, low angle grain boundary (LAGB) or high angle grain boundary (HAGB) a ‘CW/GB’ (a cell wall and/or grain boundary). The derivation of the model is described in two parts: dislocation generation formation and evolution of cell walls.

To explain the background thoughts that led to the model development and show some of the factors that need to be incorporated will we start by showing some of the main experimental observations in this work and other works. The grain size development as a function of the accumulated strain determined in this work and other works [44,45,46] of Al alloys between 99.5 and 99.99wt% purity, and low purity (97wt%) Al, are shown in Fig. 4. (Total equivalent strain during ECAP is determined using the equation described by Iwahashi et al [47] and the equivalent strain is determined using the approximation for large strains recommended by Zhilyaev and Langdon [5].) This figure shows that at strains 1 to 3 the CW/GB size is very different between the different alloys

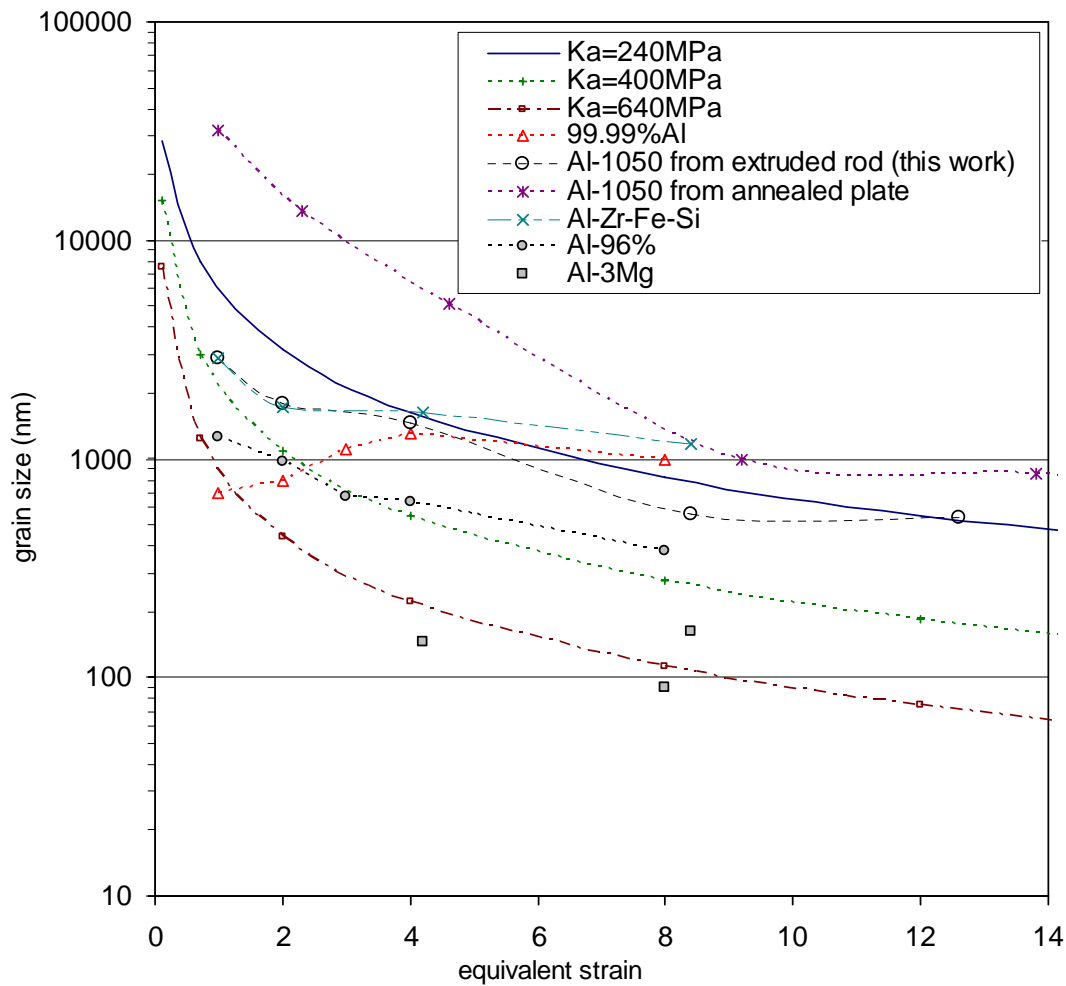


Fig. 4 Measured grain size as a function of the equivalent strain for several ECAP processed alloys. See text for details. The curves present model predictions valid for strains larger than 3 (see Section 3.3). Data for Al-97%, Al-3Mg and Al-99.99% obtained from TEM and EBSD data in [45,46, 75,98]. Data on ECAP processed Al-1050 annealed plate from [104].

. However, for the alloys with purity higher than 99.5wt%, from strain about 3 to 4, CW/GB size tend to converge to about 1000 nm at strain 8 with a slight tendency for decreasing CW/GB with increasing

strain. The CW/GB size of 97wt% pure Al alloy, however, does not converge with the others and the grain size (about 400 nm) is markedly smaller than the higher purity alloys. Al-Mg alloys (Mg contents between 3 and 6%) achieve grain sizes that are much finer, at about 100nm. Also the presence of intermetallic particles has been shown to cause enhanced grain refinement [36]. Both dissolved Mg and undissolved intermetallic particles are known to enhance dislocation generation during plastic deformation [21,48].

This short survey of some of the data indicates that differences in dislocation generation rate are correlated with grain size after SPD. Thus dislocation generation is a main element of the present model, which aims to describe the grain sizes achieved in the range of strains above 3.

3.2 Dislocation generation

In the classic theories of dislocation generation and movement in crystals, existing dislocations move and new ones are generated (for instance at Frank-Read sources or at grain boundaries) and they travel through the crystal until their movement is blocked by an obstacle, which can be another dislocation, a grain boundary, or a second phase particle. In the Kocks-Mecking (KM) [49,50,51] approach, the athermal storage of moving dislocations is taken to be determined by the average spacing between the dislocations (i.e. $\rho^{-1/2}$). The evolution equation takes the following form:

$$\frac{d\rho}{d\gamma} = k_1\rho^{1/2} - k_2\rho \quad (1)$$

The first term describes the increase in dislocation generation rate due to increase in obstacle density caused by dislocation storage. The second term considers dislocation density change due to dislocation annihilation. If the dislocation storage term dominates then the dislocation density increases as γ^2 . This would lead to strength increasing linearly with strain, because the CRSS increment due to dislocations $\Delta\tau_D$ increases with $\rho^{1/2}$ [52,53]:

$$\Delta\tau_D = \alpha_1 G b \sqrt{\rho} \quad (2)$$

where α_1 is about 0.3, G is the shear modulus, b is the Burger's vector. Whilst some large grained pure metals or single grain materials may exhibit this linear hardening behaviour over a small range of strains (often termed stage II), in fact the vast majority of polycrystalline FCC metals and alloys, including virtually all alloys with a commercial relevance, behave in different ways. To incorporate this, the evolution equation was modified to include a mean free path for dislocation movement, l_d , which provides the following form for the dislocation generation [54]:

$$\frac{d\rho}{d\gamma} = (bl_d)^{-1} - k_2\rho \quad (3)$$

If the mean free path term dominates and is about constant, the strength will increase proportional to square root of strain. This relationship is:

$$\Delta\tau = G\alpha_1\sqrt{\frac{b}{l_d}}\sqrt{\gamma} \quad (4)$$

Employing the notion that for a polycrystal the average plastic stress, ε_p , and average shear stresses on slip planes are proportional with proportionality constant, M , the crystallographic orientation factor (often termed the Taylor factor), i.e. $\varepsilon_p = \gamma.M$, provides:

$$\begin{aligned} \Delta\sigma &= G\alpha_1\sqrt{\frac{Mb}{l_d}}\sqrt{\varepsilon_p} \\ &= K_A\sqrt{\varepsilon_p} \end{aligned} \quad (5)$$

where K_A is an alloy-dependent constant. This strength increase proportional to square root of strain (a parabolic stress strain curve) has been observed in a range of plastically non-homogeneous materials including polycrystalline materials [21]. This proportionality is only valid over a limited strain range, which is alloy dependent and has been estimated to be between about 0.01 to 0.05 [21,55].

In the literature, the occurrence of a parabolic stress-strain curve has been related to non-shearable particles in the material, which are the direct micromechanical cause for a mean free path for dislocation movement, l_d , and which dominates dislocation generation leading to Eq. 3-5. To develop our model for grain size, we will first expand the theory related to the parabolic hardening curve. To this end we first obtain K_A experimentally from stress-strain curves for plastic strains 0.01 to 0.05. (It is noted K_A may also be estimated from measured work hardening exponents using a conversion described in [55]).

To develop a simple model for K_A we proceed as follows. The increase in K_A due to non shearable particles was given as [21]:

$$K_{A,ns0} = C_2G\left(\frac{fbM}{2r}\right)^{1/2} \quad (6)$$

Alloy / heat treatment	Zn	Li	Cu	Mg	Mn	Zr	K_A meas (MPa)	K_A model (MPa)	Source / data
1050	0	0	0.02	0.02	0.02	0	240	225	determined from data in [56]
Al-3Cu-0.5Mg-0.4Mn	0	0	2.72	0.45	0.43	0	350	352	this work
Al-3Cu-1Mg-0.4Mn	0	0	2.81	1.05	0.4	0	350	354	this work
Al-1Mg-2Cu-2Li-0.1Zr	0	1.56	2.27	1.03	0	0.106	370	361	this work
Al-1.6Mg-4Cu-0.3Mn	0	1.6	2.24	0.94	0.42	0	330	341	this work
Al-4Cu-1.4Mg	0	0	4.3	1.37	0.42	0	430	407	this work
Al-1Mg-0.3Mn	0	0	0	1	0.25	0	430	457	this work
Al-2Mg-0.3Mn	0	0	0	2	0.25	0	570	562	this work
Al-3Mg-0.3Mn	0	0	0	3	0.25	0	630	628	this work
Al-1Mg-0.2Cu-0.3Mn	0	0	0.02	1	0.25	0	440	457	this work
Al-2Mg-0.2Cu-0.3Mn	0	0	0.02	2	0.25	0	580	562	this work
Al-3Mg-0.2Cu-0.3Mn	0	0	0.02	3	0.25	0	620	628	this work
Al-1Mg-0.4Cu-0.3Mn	0	0	0.04	1	0.25	0	440	457	this work
Al-2Mg-0.4Cu-0.3Mn	0	0	0.04	2	0.25	0	580	562	this work
Al-3Mg-0.4Cu-0.3Mn	0	0	0.04	2.9	0.25	0	620	620	this work
7150 T6	6.2	0	1.9	2.3	0	0.12	390	374	Kamp et al [55]
7150 T7651	6.2	0	1.9	2.3	0	0.12	440	402	Kamp et al [55]
7449 T6	8	0	1.9	2.3	0	0.12	370	374	Kamp et al [55]
7449 T7651	8	0	1.9	2.3	0	0.12	390	414	Kamp et al [55]

Table 2 Compositions (in wt%) of alloys tested by uniaxial tensile or compression tests, with K_A values determined from the tests. (Data on Al-1050 obtained from [56]) Predicted values of K_A were obtained from the model outlined in the section 3.2. Accuracy of experimental K_A determinations is typically ± 15 MPa.

where C_2 is a constant equalling about 0.25 [21]. From measured K_A values (determined in this work and from the literature [55,56]) in Table 2 it can be seen that Mg considerably increases K_A . In the alloys concerned Mg is dissolved in the FCC Al phase. The effect of Mg addition on work hardening and dislocation generation has been studied extensively and a range of possible explanations have been provided [48,57,58,59]; these explanations include a modification of stacking fault energy (SFE) and changes in substructure formation rate through Mg additions. However, there is no general agreement in the literature on these mechanisms (see e.g. discussion on SFE effects in [57]), and no consistent predictive model linking dislocation generation to solute content is available. Below we will propose such a model. To explain the origins of that model, we first observe that from a comparison of measured dislocation densities in deformed pure Al and binary Al-3Mg it was shown that Mg addition drastically increases the dislocation density [48]. It has also been shown that for a range of solution treated Al-Mg-Cu alloys the work hardening increases proportional to the Mg content [38], suggesting that K_A increases linearly with amount of Mg dissolved in the Al rich phase. We observe that these (and other) observations can be explained by considering that the formation of Mg-Mg nearest neighbour pairs is energetically unfavourable and effectively introduces an increase in free energy which acts as an effective force against the movement of dislocations through the lattice. Whilst the origin is very different from the mean free path due to geometrical obstacles, also the local free energy

effect due to nearest neighbour pairs can effectively be described through a mean free path of dislocations. We will term this effective mean free path of dislocations due to chemical bonds related to dissolved elements the effective chemical mean free path, l_{ch} . We may consider the mean free path due to geometrical obstacles, l_g , as caused by hard, non shearable objects, whilst the effective chemical mean free path, l_{ch} , is a consequence of the raising of free energy of the lattice in the wake of a moving dislocation (see discussion).

Both l_{ch} and the mean free path due to geometrical obstacles, l_g , will cause an increase in dislocation density on deformation. As we will show below, the dislocation generation capability of these two effects is of similar order of magnitude, and we approximate the superposition in a similar way as in precipitate-dislocation interaction theory for obstacles of similar strength [60,61], i.e. using a quadratic superposition rule.. The superposition rule for l_{ch} and the mean free path due to geometrical obstacles, l_g , will be $l_d^{-2} = l_{ch}^{-2} + l_g^{-2}$ and hence we obtain:

$$K_A = C_2 GM^{1/2} b^{1/2} (l_g^{-2} + l_{ch}^{-2})^{1/4} + K_A^0 \quad (7)$$

where K_A^0 is the contribution due to generation of dislocations unrelated to geometrical or chemical obstacles. For (approximately) spherical obstacles in an alloy with dissolved alloying elements i , at concentrations x_i this gives:

$$K_A = C_2 GM^{1/2} b^{1/2} \left(\left[\frac{f}{2r} \right]^2 + \sum [B_i x_i]^2 \right)^{1/4} + K_A^0 \quad (8)$$

where B_i are constants. We applied the latter equation to fit K_A values for the 20 alloys listed in Table 2, using measurements and predictions of f (based on known phase diagrams) and r (as obtained from TEM and SEM data, and further data and estimates in [62,63,64,65,66]) and by subsequently fitting B_{Mg} and K_A^0 . (The calculation and predictions of f and r are outlined in the appendix.) This provided a fit with root mean square error (RMSE) 17.2 MPa. This is within the experimental accuracy, and hence this fit is fully satisfactory and supports the latter equation. (Fitting C_2 , B_{Mg} and K_A^0 together provides a RMSE that improves to 17.0 MPa and C_2 is determined to be 0.27, which nearly indistinguishable from the value determined by Ashby [21].)

Using the above model allows us to describe the amount of dislocations generated during deformation up to a strain of 5% as:

$$\rho_g = \gamma \left(M \left[\frac{Gb\alpha_1}{K_A} \right]^2 \right)^{-1} \quad (9)$$

where ρ_g is the total amount of dislocations per volume unit generated since the start of deformation. We now make the assumption that the total amount of dislocations generated in the SPD regime (strains in excess of 3) is reached is given by the same equation, with one modification: we will take account of particle breakup by taking the particle size to be the one in the SPD regime. The latter two equations then provide a full description of the amount of dislocations generated as a function of composition, amount and size of non shearable particles and b , G , α_1 , and are key elements of our model for grain size prediction.

3.3 Formation of grain boundaries

Moving dislocations will follow different paths. In the cold deformation considered here they have only 4 destinations: they can be

- mobile dislocations in the grain,
- immobile dislocations in the grain,
- in cell walls and/or grain boundaries,
- annihilated within the grain, for instance by recombination of dissociated dislocations through cross-slip.

Several models have been proposed to account for the evolution of these dislocation groups (see e.g. [41,43,51,67]). We will here develop a description that uses elements of these, but, to achieve transparency, we will simplify them to incorporate only the elements that are relevant to describe grain structure refinement at the very high strains encountered in SPD.

Annihilation of dislocation within a grain has been mentioned extensively in the literature. However, here we want to explore the simplified and computationally efficient model that can be derived by assuming any annihilation of dislocations within a grain is too limited to affect grain refinement. This may be justified as there is no proof that in alloys severely plastically deformed at temperatures typical for cold deformation this would occur on a significant scale. We will discuss this issue in section 5.8. Thus the changes in the amounts of dislocations are here described as:

$$\rho_{gen} = \rho_{GB} + \rho_G \quad (10)$$

For cell walls, the misorientation between two neighbouring cells is dependent on the density of dislocations as [68,69]:

$$\rho_{cw} = 1.5 S_v \theta / b \quad (11)$$

where S_v is the area of boundaries per unit volume and θ is the wall misorientation angle (in radians). We will assume (see discussion) that this holds for any grain boundary, and hence it follows:

$$\rho_{GB} = \int 1.5 \frac{\theta}{b} dS_{v,def} \cong 1.5 \frac{\bar{\theta}}{b} S_v \quad (12)$$

It is readily shown that for SPD $\rho_G \ll \rho_{gen}$, hence the dislocation density in the grain, ρ_G , can be neglected (see discussion). As the total area of boundaries per unit volume is given by:

$$S_v = S_{v,def} + S_{v,o} \quad (13)$$

we can write:

$$\rho_{GB} = \gamma \left(M \left[\frac{Gb\alpha_1}{K_A} \right]^2 \right)^{-1} \cong 1.5 \frac{\bar{\theta}}{b} (S_{v,def} + S_{v,o}) \quad (14)$$

S_v is related to the mean linear intercept length, \bar{L} , via the fundamental relationship $S_v = 2/\bar{L}$ [37,70]. There are a range of ways in which an ‘average’ grain size can be defined [37]. Although sometimes \bar{L} has been taken as ‘grain size’, we will here take the grain size, d , to mean $V^{1/3}$, where V is the average volume of a grain. S_v is inversely proportional to an average grain size, d , and if we make an assumption on the shape of grains and the distribution of sizes we can relate d to S_v and \bar{L} . The present model does not make a prediction of grain shapes, however the stochastic nature of distribution of the objects causing dislocation multiplication leads us to believe that the distribution of grain shapes is likely to resemble that of a Poisson-Voronoi one, and hence [71]:

$$S_v = 2.91/d \quad (15)$$

and

$$d = 1.455 \bar{L} \quad (16)$$

(For comparison, if grains are cubes $S_v = 3/d$, or if grains are β -tetrakaidecahedrons $S_v = 2.77/d$. For a Johnson-Mehl type distribution $S_v = 2.57/d$, but grain structures created by SPD are different from recrystallised structures and hence this appears a less realistic than a Poisson-Voronoi one. Throughout this paper we will report d values defined by the latter two equations, thus \bar{L} values can be directly calculated from reported d values.)

Thus we can obtain the grain size, providing we can find a suitable value for $\bar{\theta}$. From comparison of $p(\theta)$ distributions for several alloys processed between 4 to 12 passes of ECAP in our $\Phi = 90^\circ$ die ([35]), we can determine $\bar{\theta}$. $\bar{\theta}$ does not show a substantial dependence on alloy composition, and varies only little with amount of accumulated strain for strain in excess of 3. The average for our Al1050, Al-Zr, Al-Si-Fe-Zr and Al7034 deformed by ECAP to strains between 4 and 8.4 (and up to 12 for the

Al1050 alloy) is determined as $\bar{\theta} = 27.1^\circ$. (For comparison, for a polycrystal with a randomly oriented grains $\bar{\theta} = 40.7^\circ$ [72].)

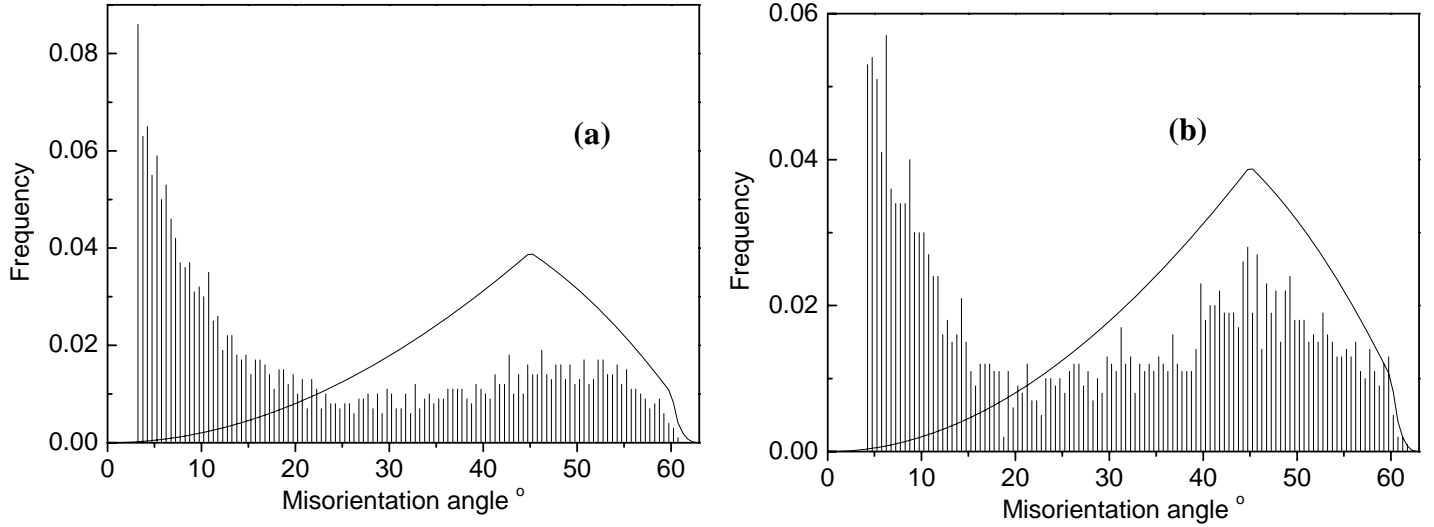


Fig. 5 Misorientation distribution of (a) an AA1050 alloy and (b) AlZr alloy processed by ECAP (4 passes). The average misorientations are 20.8° and 24.6° , respectively. The solid lines are the theoretical distributions for a polycrystal with a randomly oriented grains [72].

If the starting grain size is large, the equations further simplify to:

$$d \cong 2.91 / S_{v,def} = 1.5 * 2.91 \frac{\bar{\theta}}{\rho_{GB} b} \quad (17)$$

4. Results and analysis: Grain size during SPD

We have tested the present model for grain size evolution by comparison of its predictions to a range of data on grain size of SPD Al alloys. New data was obtained by performing ECAP on Al-1050, Al-Zr and Al-Zr-Si-Fe alloys and HPT on Al-2024 and Al-3Mg-0.2Mn, TEM and SEM micrographs for several alloys processed by ECAP and HPT are presented in Figs 6-8. Grain size data for a range of other commercial and experimental alloys was obtained from [30,35,36,73,74,75,76,77,78]. The database contains a total of 21 alloys, in a total of 37 alloy-processing combinations, with strains ranging from 1 to 17 and with resulting grain sizes between 2 μm and 50 nm, the full database is presented at [79]. Having determined $\bar{\theta}$ from EBSD data and K_A from the work hardening model, there

are no fittable parameters in the model for grain size prediction. The results are presented in Figs 9 and 10. The model accuracy in terms of average percentage accuracy is 22%. In line with the present model it has been found that additions of Sc and Zr to Al-Mg have little effect on the grain size after HPT (although these additions do significantly reduce grain growth on annealing after HPT) [75].

No data was eliminated from consideration other than ECAP procedures leading to very much elongated grains in the route A processing of Al-Sc alloys in [80] which are not considered here and alloys containing extensive amounts of precipitates that induce planar slip, such as Al-Li based alloys [81,82] (see Discussion). 99.99wt% pure Al shows trends in grain size evolution that are very different from the alloys considered. This was to be expected because, as mentioned, the assumption of parabolic hardening that is key to the present model is not valid for high purity metals. It will be further discussed in section 5.5.

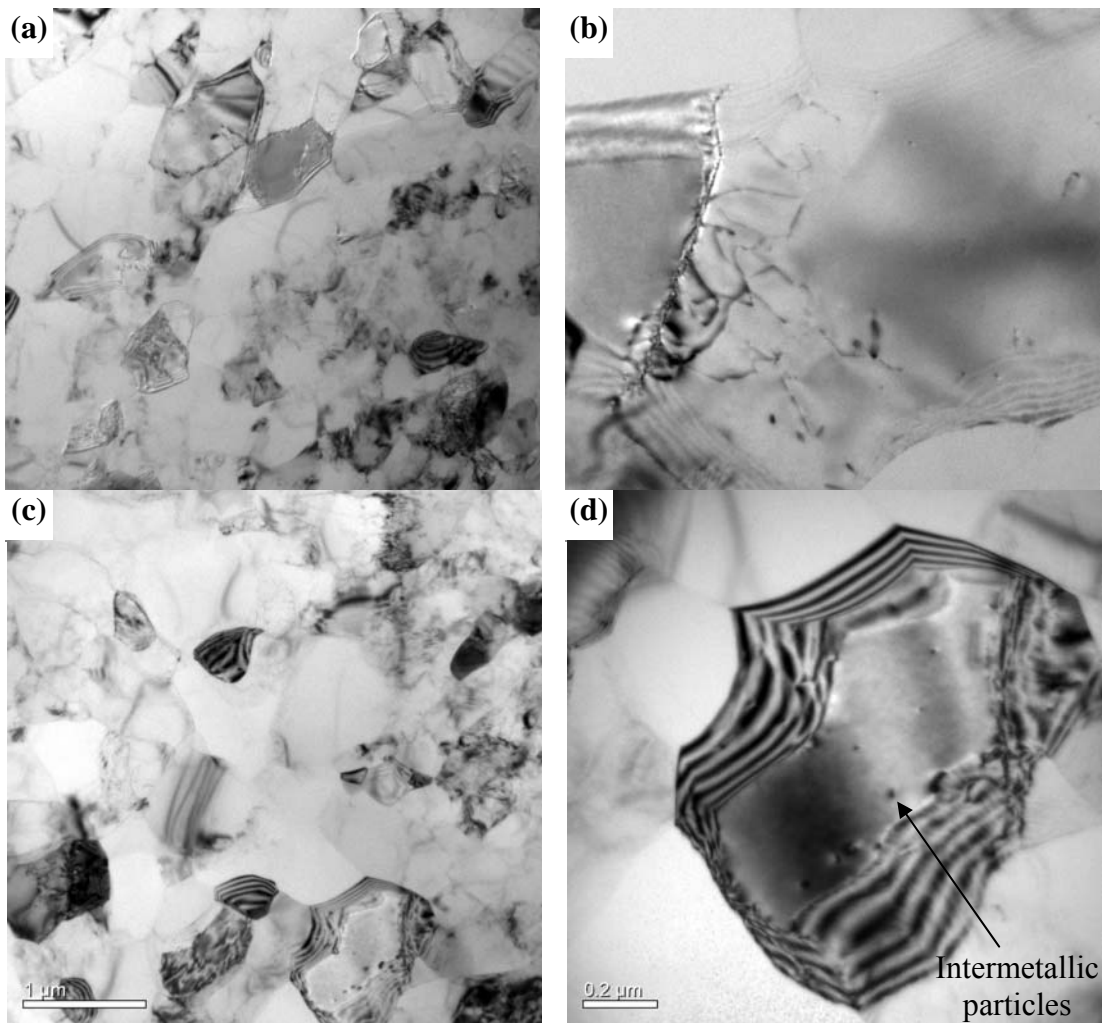


Fig. 6 TEM micrographs of a selection of ECA processed alloys. AlZr alloy after (a), (b) 4 and (c), (d) 8 passes of ECAP.

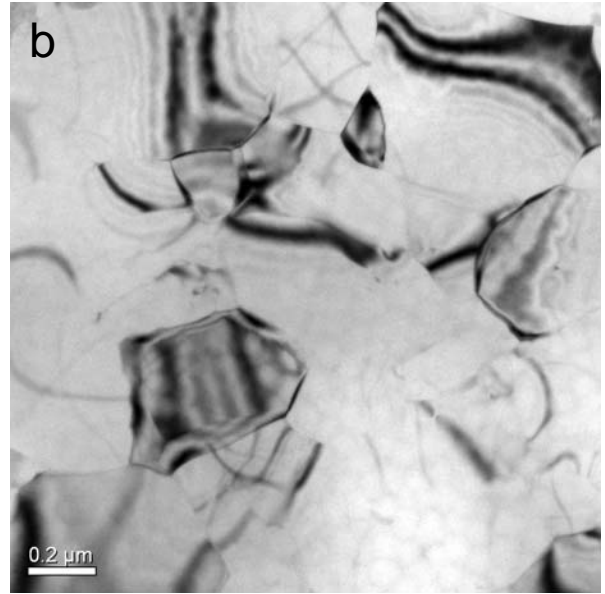
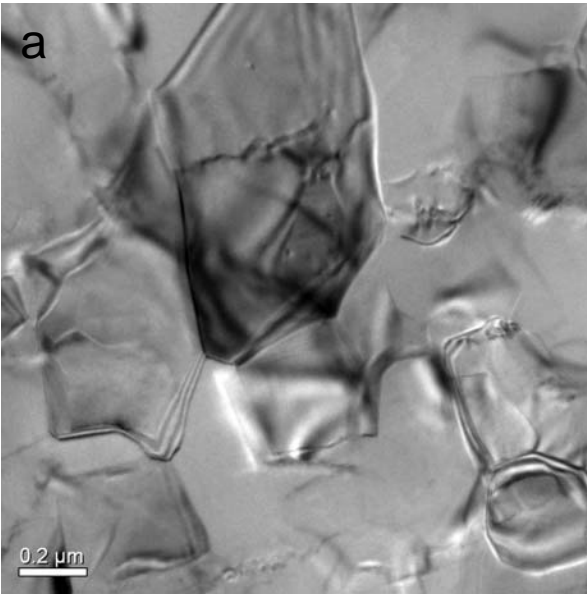


Fig. 7 TEM micrographs Al 1050 processed by HPT for 5 turns: a) at 2.5mm position from center of disk ($\epsilon_{eq} \approx 5.30$); b) at 4mm position from center of disk ($\epsilon_{eq} \approx 5.84$).

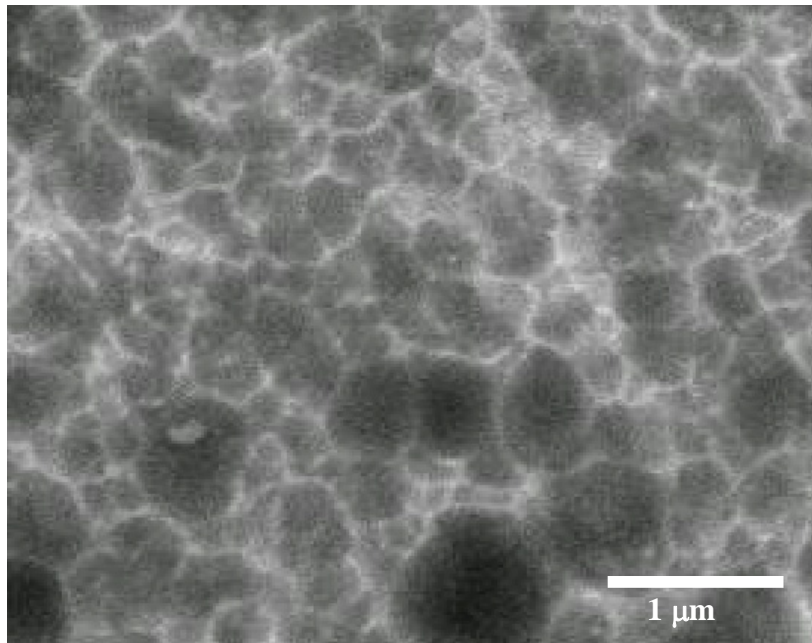


Fig. 8 SEM micrograph (secondary electron mode) of an Al-3Mg-0.4Mn sample HPT processed by 2 turns to $\epsilon_{eq} = 4.1$. (Polished sample etched in Keller's reagent). Dimpled appearance of part of the surface is thought to be due to preferential etching of clusters of grains with crystallographic orientations prone to etching. Measured average grain size is 280 ± 30 nm.

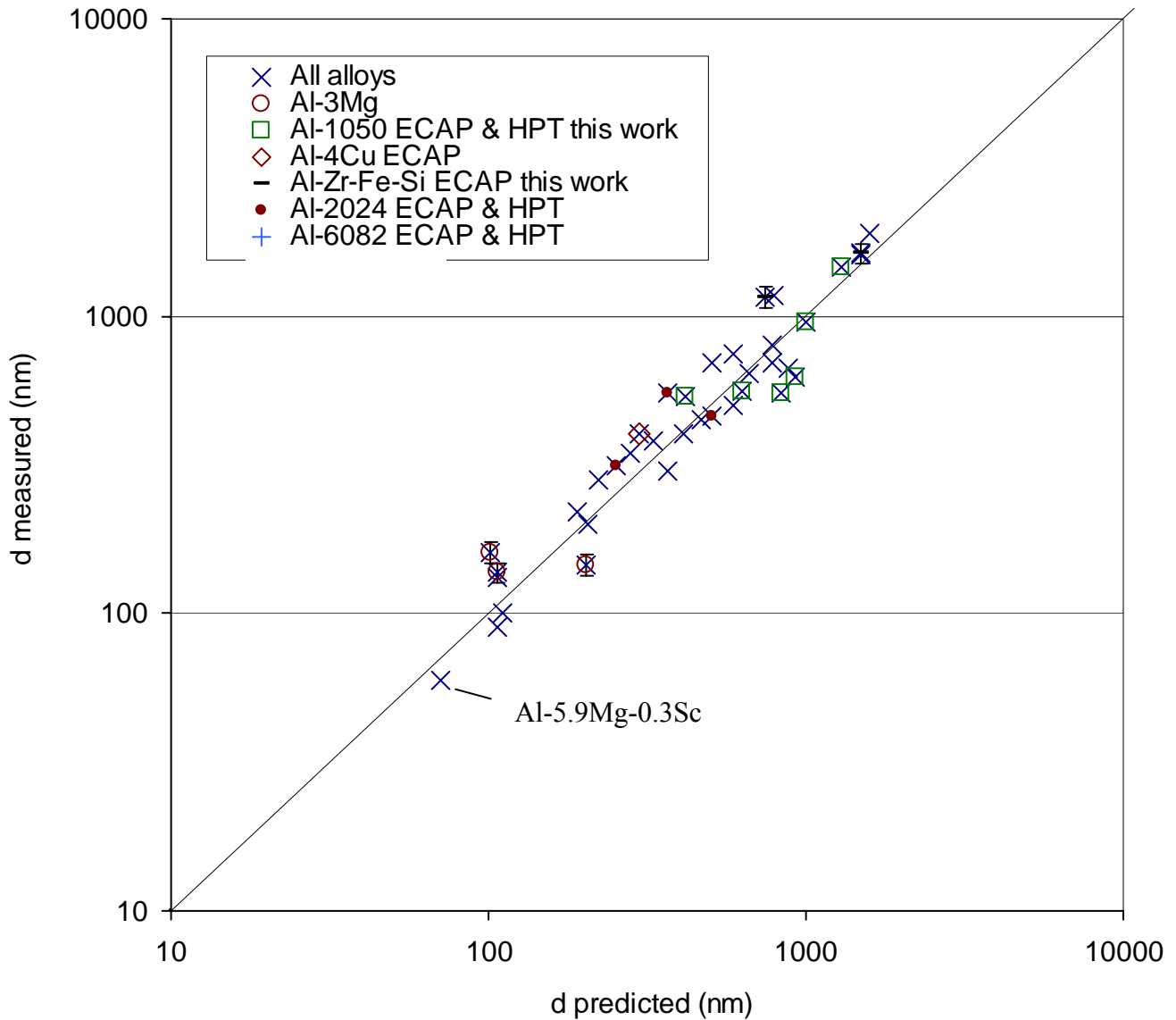


Fig. 9 Measured and predicted grain size of a range of Al alloys subjected to ECAP or HPT for total equivalent strains in excess of 3. Grain sizes were calculated from EBSD data (misorientation angles $> 2^\circ$), TEM or SEM.

5 Discussion

5.1 Mechanism determining grain refinement at large strains: why do the simplifications work?

The present model makes a number of assumptions and simplifications that at first glance seem at odds with the complexity involved in microstructural evolution during cold work shown in the literature (see e.g. [83]) and also avoids elements of other models (e.g. [41,43,84]). It needs to be noted here that these more complex models are generally targeted at explaining the different stages of deformation starting from low strains. The present model is different in that we do not attempt to capture the details

of 3D progressive microstructure development starting at low strains, but instead look for the overall material-averaged parameters that are the main factors in determining the density of grain boundaries once the average grain boundary misorientation angles start to approach a near stationary value. Thus the model includes simplifications and assumptions that are valid for the very high strains typical of SPD, and is successful for these conditions through identification of the mechanisms that are the main determining factors for dislocation generation and grain boundary formation.

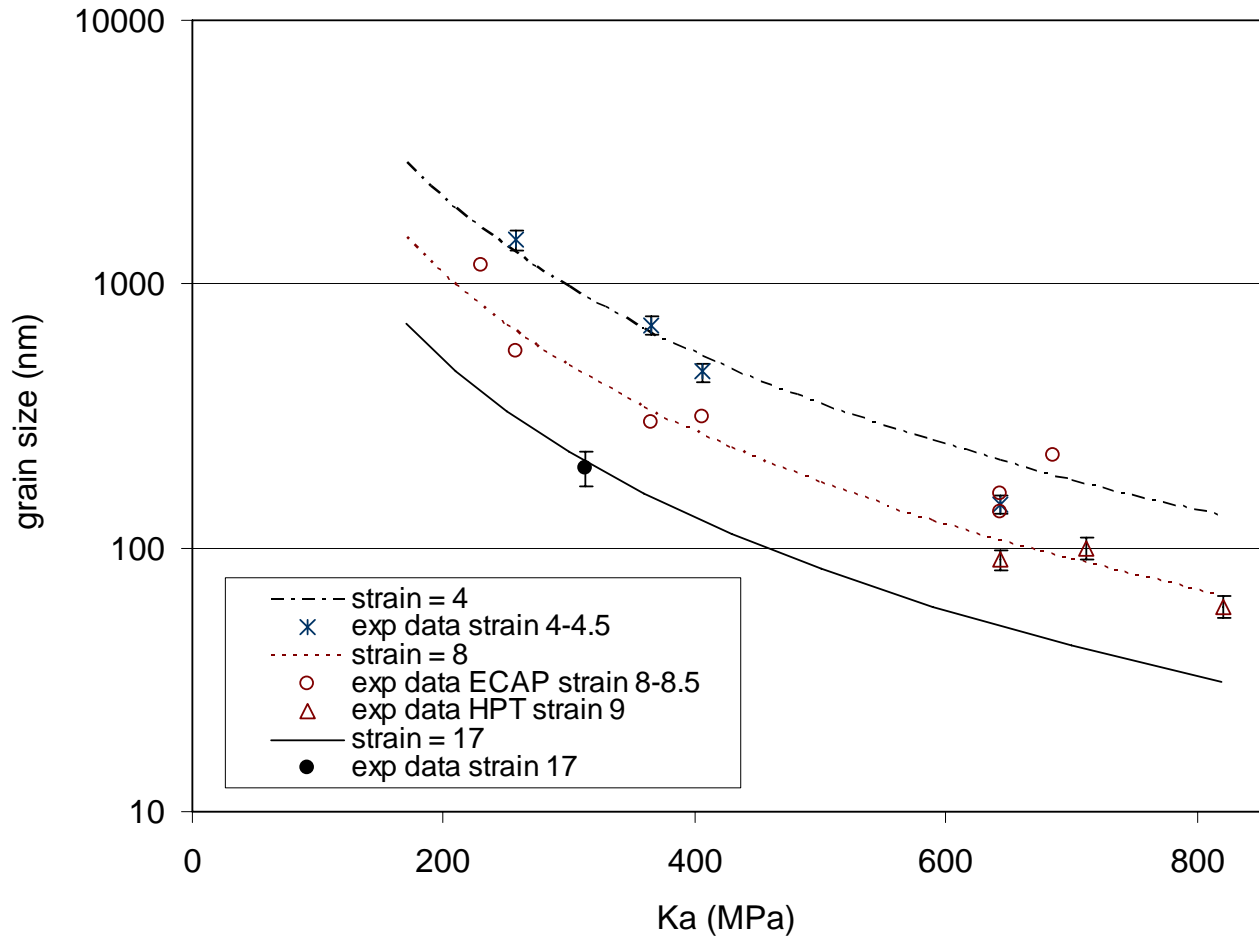


Fig. 10 Predicted (lines) and measured (symbols) grain size of a range of Al alloys subjected to ECAP as a function of work hardening factor K_A .

As grain size gets progressively refined, the dislocations created due to the presence of non shearable particles will start to arrive at grain boundaries in ever greater numbers. These dislocations are geometrically necessary in the sense that they are required to create deformation at the non-shearable particle, but they are in general not geometrically necessary in terms of the misorientation angle of the grain boundary. Thus a part of these dislocations will not contribute to misorientation of the grain

boundary, and a constellation sometimes described as non equilibrium boundary will result. Thus non-equilibrium boundaries, often observed in SPD metals, are a natural consequence of SPD in the present model.

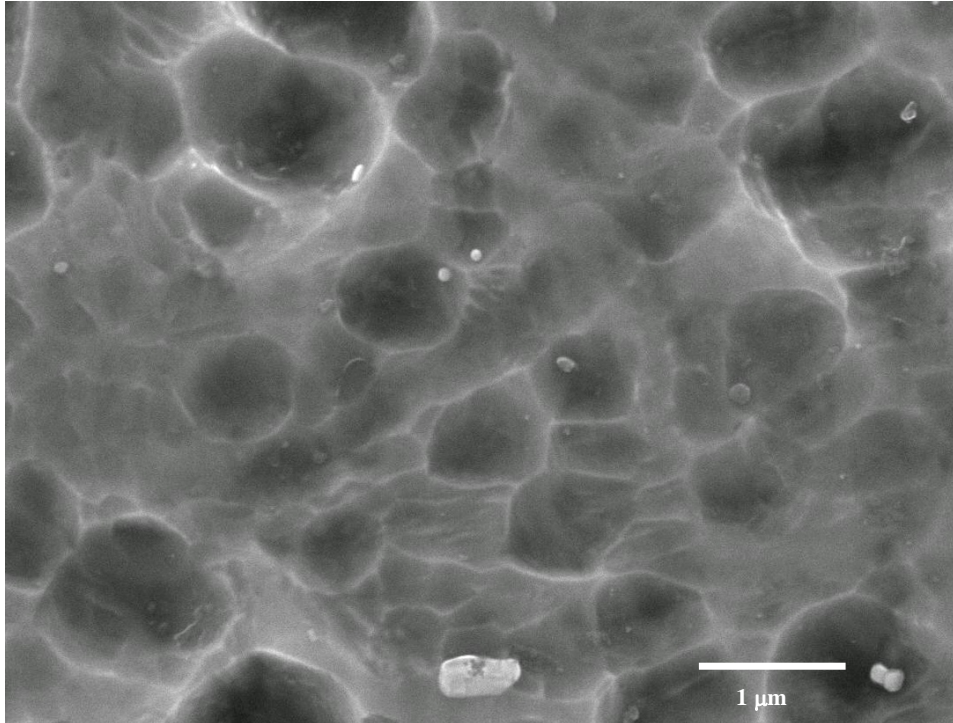


Fig. 11 FEG-SEM micrograph of Al-1050 processed by HPT to an equivalent strain of ~ 4 (2 turns). Sample was polished and etched to reveal the intermetallic particles. Dimpled appearance is thought to be due to preferential etching of grains or clusters of grains with crystallographic orientations prone to etching.

In the model we considered that $\rho_G \ll \rho_{gen}$ and proceeded to ignore ρ_G . To support this we have obtained dislocation densities for a range of Al based alloys subjected to SPD from a number of investigations [30,46,53,48,85,86,87] and compared this with ρ_{gen} according to the model. The dislocation densities were measured through x-ray diffraction (XRD) line broadening analysis or TEM. Data presented in Table 3 support that for $\epsilon > 2$, $\rho_G \ll \rho_{gen}$ is valid. In our own TEM experiments on Al-Zr (see Fig.6c,d) we find dislocation densities that are even lower, lower than $10^{14}/m^2$ and also other TEM work on SPD alloys have shown dislocation densities in grains that are as low or lower than this [24]. Thus, whilst refining the model by predicting ρ_G might slightly improve the accuracy of the model, the relative benefit of such an expansion of the model is very limited.

The present model provides a direct quantitative explanation of the effect of Mg additions on grain refinement from the effect Mg has on dislocation multiplication. The effect of Mg on grain refinement has been discussed before and it was suggested that reduction in recovery rate by Mg additions is a main cause [88]. Mg, as well as a range of other alloying additions, may well reduce recovery rates in the temperature ranges where recovery occurs, however, the present model suggests that this is not the main cause for the effect of Mg additions on grain refinement. Two further observations support this view. Firstly, the absence of strain rate effects in SPD indicates that recovery during SPD is not significant. Secondly, measurable hardness reductions due to recovery, occur at temperatures above 250°C [89], which is well in excess of the temperatures considered here.

Alloy	Process	ϵ	$\rho \times 10^{14} \text{ m}^{-2}$		Method	Ref
			meas	total pred		
Al-3Mg-0.4Cu	Cold roll	0.1	2.7	10	TEM	53
Al-3Mg-0.4Cu	Cold roll	0.6	5	18	TEM	53
Al-6082	ECAP	1.0	4	18	XRD	86
Al-7075	ECAP	2.0	9.4	142	TEM	85
Al 97wt%	ECAP	4.0	3.8	118	TEM	46
Al-1Mg	ECAP	6.0	4	280	XRD	87
Al-3Mg	ECAP	4.0	27	389	XRD	48
Al-7Si	ECAP	7.0	1	168	TEM	30

Table 3: Measured dislocation density for several Al alloys subjected to cold deformation (incl SPD) and the total amount of dislocations generated per volume according to the present model.

5.2 Aspects of grain boundary evolution not included in the present model

The success of the simplified model does not mean that other details of deformation mechanisms are not relevant in broader understanding. For instance the character of defects defining deformation (edge or screw dislocations, prismatic loops, stacking faults, non-equilibrium grain boundaries) and orientations of slip and cell walls is relevant, but ultimately the grain refinement process at these high strains can be described well considering just a generic type of dislocations and a generic cell wall / grain boundary. It is also worth noting that continuous increase of $\bar{\theta}$ with strain, which appears to follow a power law for strains up to 4 [90], will have to end as $\bar{\theta}$ approaches 25°, as most grain misorientation angles are beyond the point where crystal symmetry starts affecting the distribution (at 25°). For the same reason also the scaling behaviour of the GB misorientation angle observed at relatively low strains [91], can not be valid at the high strains considered here. Thus in assessing the

present model on needs to be aware that this behaviour observed at lower strain can not be extrapolated to the high strains encountered in SPD. The present model effectively assumes a saturation misorientation angle is reached in the SPD regime. The latter is in line with data on SPD through multi-directional forging of Al-7475 at temperatures from 300°C, where the average grain boundary misorientation angle reaches a saturation angle of about 31° for strains of about 6 [92]. ECAP at 250°C on Al-2219 results in $\bar{\theta}$ values that saturate at about 25 to 30° in the SPD regime [93], and for Al-6% Mg-0.3% Sc-0.4% Mn processed at 300°C similar saturation values for $\bar{\theta}$ were found [94]. It is also relevant to point out that whilst at low strains ($\ll 1$) only a small fraction of atom bonds have been broken by the passing of dislocations, the SPD regime ($\epsilon > 3$) is characterised by a cumulative number of bond breaking events that is larger than the total number of bonds in the lattice. This is yet another reason why behaviour at low strains is likely to be different at higher strains.

The model also does not consider geometry of main macroscopic slip directions in ECAP, such as described in the work by Xu, Langdon and co-workers [25,25]. The latter description is relevant, and explains qualitatively formation of non-equiaxed grains in some SPD processing routes (for instance route A in ECAP). However, the present model indicates that as long as no redundant shear is created, the grain size evolution is described well by considering total dislocation contents without the need to describe the geometry of the main macroscopic slip directions or the crystallographic slip directions.

The present model is not successful in predicting the grain size of Al-2.2Li-5.5Mg alloys, which have inhomogeneous grain sizes with an average grain size that is 10 times as large as the current predictions. In retrospect this should come as no surprise as Li contents in excess of 1.5 wt% contain δ' precipitates, which induce inhomogeneous, planar slip, which would cause the creation of cell walls to be concentrated in well spaced shear bands, thus invalidating the implicit assumptions in the model that there is no lower limit to the cell size. The reported exceptionally small grain size (<100 nm) of HPT processed highly alloyed, solution treated and aged (T6) Al-7.5%Zn-2.7%Mg-2.3%Cu-0.15%Zr alloy [95] is consistent with our model, if we estimate the precipitate diameter to be about 10 nm, which is reasonable in the light of data in [65], with a volume fraction of about 0.07 [65].

5.3 An alternative view of grain refinement: subsuming of dislocations and rotation.

An alternative means of justifying main concepts in the model is the following. In common with a range of processes, the evolution of deformation and grain structure refinement during HPT involves the creation of a state with high energy (mainly through a high dislocation density) that reduces its free energy through a relaxation process. In many relaxation processes the relaxation mechanism that dominate can be seen as being the ones that can occur the fastest, which means a straightforward combination of processes. Now consider through which simple imaginary geometric operations we can produce, starting from a coarse grained material, a refined microstructure that captures the main elements of a real microstructure after HPT. The simplest way appears to be through two operations:

- define the locations of new GBs; for instance a Poisson-Voronoi tessellation seems a reasonable method
- produce a random grain rotation for each grain.

The amount of dislocation assimilated in the grain boundaries will depend on the average grain boundary misorientation and S_v (a similar point is made in [96]) Thus, if nearly all dislocations generated are assimilated in the GBs, S_v will depend only on the average grain boundary misorientation and the total amount of dislocations generated in the cause of deformation processing.

Whilst this reasoning is by no means a proof, it does provide an unintuitive framework that leads provides the same basic equations as the model derived above.

5.4 Influence of dissolved atoms on dislocation generation

Several types of dissolved atoms in FCC metals, particularly Mg in Al are known to have a significant influence on the work hardening rate of alloys. In the present model we incorporate this effect by considering that the dissolved atoms increase the generation of dislocations on plastic deformation, and we introduce the concept of dislocations induced by local free energy effects (we may term this ‘chemically necessary dislocation’). The model shows that this concept fits the experimental data on work hardening and on grain size well. We will here discuss mechanisms and subsequently consider available microstructural evidence.

Consider atoms of type A (for instance Mg) dissolved in a lattice of host metal M (for instance FCC Al). The A-A near neighbour bonds have a positive interaction energy, i.e. they repel each other. Apart from A-A near neighbour pairs being avoided, the A atoms are distributed randomly in the lattice of host metal M. When a single dislocation passes through the lattice some new A-A nearest neighbour pairs will be created. Depending on the type of atom involved these near neighbour pairs can be energetically unfavourable, and if the associated free energy increase is sufficiently large, a process of generation of an additional dislocation can occur. Different alloying elements will have different A-A interaction energies and hence have different propensity for additional dislocation generation. Mg dissolved in Al will have a high propensity as it is known that at sufficiently high Mg contents an $L1_2$ ordering will occur [97] (ultimately leading to the $L1_2$ ordered Al_3Mg phase), which is characterised by having no Mg atoms on nearest neighbour positions. Another element with $L1_2$ ordering propensity in FCC Al is Li.

At present, direct microstructural evidence for the mechanism described above is lacking. This kind of evidence is expected to be impossible to obtain, as there is no single technique that can detect a dislocation and a solute atom. However there is indirect evidence. As noted above, a comparison of measured dislocation densities in severely deformed pure Al and Al-3Mg in [48] has shown that Mg addition increases the dislocation density. HREM on an Al-1.5Mg alloy plastically deformed through

HPT to a strain of about 7 has revealed a high density of defects each made up of terminations of a (111) and a (200) fringe within grains [98]. Such unusual defects have hitherto not been explained. The defects are consistent with the above mechanism for chemically necessary dislocations: the introduction of such a dislocation pair will change the local atomic arrangement such that Mg-Mg nearest neighbour formation is avoided when a dislocation induced by plastic deformation of the grain travels in between the two Mg atoms in such a way that it would form the Mg-Mg nearest neighbour formation.

5.5 Pure FCC metals

Much of the detailed TEM and EBSD work microstructure evolution on in cold-rolled Al alloys was performed on high purity Al and also much of the early work on microstructure evolution on in ECA processing of Al alloys was performed on high purity Al. However, there is a range of differences between pure FCC metals and their alloys. 99.99% pure Al has a grain refinement behaviour that is substantially different from that of Al alloys. Also the hardening behaviour with increasing strain in HPT is also vastly different: Al softens on increasing strain [99]. HPT, ECAP and cold rolling of pure Al all result in subgrain sizes that are about 0.7 to 2 μm , which is 2 to 4 times smaller than the present model. Experiments have shown that in high purity Al deformed by ECAP up to 4 passes there are hardly any HAGBs [100]. Thus the reason for deviations from the model is that in pure Al $\bar{\theta}$ is much smaller than the value of 27° that was taken in the model. Lowering $\bar{\theta}$ to about 15° to reflect the dominance of very low angle subgrain boundaries results in a good correspondence with experiments. So the basic model formulation on the basis of partitioning of dislocations holds up well, with the caveat that predictive capability for pure Al depends on deriving a prediction of $\bar{\theta}$.

5.6 Breaking up of particles and oxides layers in powder metallurgical alloys

It should also be realised that the present model assumes that both the averages sizes and volume fractions of non-shearable particles are constant during SPD. In reality this is not always the case, and especially elongated, brittle particles can be significantly broken up during SPD. Within the model formulation this will cause an increase in the work hardening factor K_A and consequently dislocation generation and grain refinement will be progressively enhanced during SPD. In the model assessment we used sizes obtained from available microstructure assessment at various stages during SPD processing, but no systematic evaluation of these size evolutions was performed or was available in the literature. The model predictions may thus on average somewhat overestimate the grain size achievable at high deformations in alloys with significant volume fractions of elongated and brittle particles, and on average somewhat overestimate the grain size at the earlier stages of SPD.

The present comparison of predicted and measured grain sizes incorporates alloys for which l_g could be determined with accuracies better than about 20%. The resulting comparison shows a good correlation.

The requirement for good accuracy of l_g meant that some data, especially for materials with $l_g < 1000\text{nm}$, was omitted from the comparison. From this data it is especially interesting to discuss a commercial purity (CP) powder metallurgical (PM) Al material cold deformed to an equivalent strain of about 1.4 [101] for which a refined grain size of about 400nm was achieved and a PM Al-6061 for which a 500nm grain size was obtained after ECAP to a strain of about 4 [102]. Both of these grain sizes are substantially smaller than comparable alloys produced by conventional casting and subsequently subjected to SPD. These PM alloys typically contain a substantial amount of Al_3O_2 particles that results from breaking up of an oxide layer of several nm thick. For the PM CP Al, oxide contents of about 3 to 10 vol% were quoted [101,103]. The available data does not allow us to obtain an accurate determination of l_g . However, our model is consistent with the observations on PM CP Al if we take $l_g = 120\text{nm}$, which is achieved for instance for $f=0.05$ and $r=3\text{nm}$. Our model is also consistent with the observations for PM Al-6061 for $l_g = 600\text{nm}$, which is achieved for instance for $f=0.05$ and $r=15\text{nm}$ (r is taken from TEM data in [102]). These values for f and r values are realistic and consistent with the limited available data, which indicates that our model is also consistent with grain refinement in PM Al alloys. Accurate predictions for these alloys however rely on accurate data on size and volume fraction of oxide particles.

5.7 Sources of experimental error

A main source of uncertainty and deviations in the comparison between measured grain size and predicted grain size appear to be down to the accuracy and consistency of the experimental grain size determination. The limits of the accuracy of grain size determination is for instance noted when two grain size determinations of Al-1050 after 8 ECAP passes in a 90° die by two groups is compared. In this paper we determined $d = 580 \pm 40 \text{ nm}$ ($\bar{L} = 400 \text{ nm}$), and this was consistent (within 8%) between TEM and EBSD determinations. However, based on EBSD data and incorporating extensive data cleaning procedures (which are different from ours) El-Danaf [104] reported a ‘cell size’ of 1000 nm and based on atomic force microscopy (AFM) data Saravanan et al [105] reported a ‘grain size’ of 620 nm. (We believe this AFM data is open to a range of interpretations, and believe the data and uncertainties are best reflected by indicating $\bar{L} \cong 570 \pm 150 \text{ nm}$.) All groups used very similar ECAP dies. Also grain sizes of Al-99.99wt% processed by ECAP as determined by two groups using TEM and very similar ECAP dies [42,45] differ by 10-30%. Also, crystallite sizes determined by XRD line broadening analysis is smaller than cell/grain size determinations by TEM, for instance for Al-3Mg the crystallite size determined by XRD is about 30% lower than cell/grain size determined by TEM [48]. It appears that limitations in experimental determinations of grain size are the main factor determining these large differences.

We also need to consider the spatial resolution of EBSD measurements. When an electron beam hits the specimen the backscattered electrons that give rise to the Kikuchi patterns will be generated from a volume of finite size. If the Kikuchi pattern is due to an area with a very low angle grain boundary or

cell wall in it, the Kikuchi line will be broadened and an average orientation may be identified, and thus the low angle boundary will not be detected. For grain boundaries with misorientations larger than a few degrees the Kikuchi pattern will not be identified (a misindexing failure [106]), which will generally also lead to underestimation of density of boundaries. We find evidence for such an effect in our database, where EBSD determinations of grain size are on average 6% larger than model predictions, whilst TEM determinations of grain size are on average 1% lower than model predictions. The net difference is 7%, which is similar to differences obtained for comparisons of TEM and EBSD determination of grain size in 99.99wt% and 99wt% pure Al subjected to cold (severe) deformation [44,46].

It is also interesting to note that a close inspection of the data and model predictions reveals that on average the model underpredicts the grain size of material processed by ECAP route B_C by about 9±4%, whilst it overpredicts the grain size of HPT processed material by about 5±7% (error defined as accuracy of mean). This might be taken to indicate that at identical equivalent strain, HPT produces an S_v that is higher than ECAP. However, as all grain size analysis for HPT processed materials is done by TEM, whilst most grain size determinations for ECAP processed materials is done by EBSD, the data does not support a definitive conclusion about any differences in efficiency of grain refining between the two SPD methods. Whilst there may be a small difference (in the order of 10%), the experimental issues relating to the accuracy of grain size determination methods need to be better understood before a confident comparison can be made.

A further source of error lies in the composition and microstructural parameters that are used to calculate K_A . Considering the typical accuracy of composition determination (0.05at% for each element), volume of particles (±10%) and size determination of non-shearable particles (±20%) we estimate the contribution to the deviation in grain size of these factors at about 6%.

The above indicates that the average deviation between predicted and measured grain size (22%) is very reasonable in terms of some of the experimental uncertainties that influence grain size determinations. Especially the accuracy of grain size measurement is seen to have a large influence.

5.8 Dynamic recovery and the maximum grain refinement achievable

In the present model all dislocations are assimilated in cell walls and grain boundaries and we neglect dynamic recovery in the sense of the disappearance of dislocations due to any other process. As a consequence the model predicts that there is no limit to grain size reductions: as the accumulated plastic strain is increased to ever more severe deformations, the total amount of dislocations generated keeps rising and more and more grain boundaries need to be formed to accommodate these dislocations. The rate of refinement reduces substantially with increasing effective strain, and this is broadly consistent with experimental data on SPD processed Al alloys (see e.g. [42,107,108]). In pure FCC metals the trend is different, and the grain refinement comes to a complete halt at strains of about 4 to 8 [109,110] and in some cases even an increase in grain size has been seen on increasing effective strain beyond 8 [110]. The drastic slowing down of grain size reduction with increasing strain is often attributed to a dynamic recovery processes (see e.g. [5]). Particularly, recombination of dissociated dislocations through cross-slip has been highlighted. If the minimum stationary grain size is governed by a balance between dislocation generation and dislocation annihilation and recombination, the minimum grain size is proportional to the square root of the stacking fault energy [111], and analysis of experimental data has shown correlations between grain size and stacking fault energy [112,113]. Data on SPD processed Cu-Al and Cu-Zn alloys also shows increase in solute content drastically reduces grain size [112,113]. Whilst this data has been interpreted in terms of the stacking fault energy [112,113], it is noted that the observed influence of alloying elements is also consistent with our model. Consistent with the occurrence of dynamic recovery at very high strain, our model does indeed have a tendency to overpredict the grain refinement at very high effective strains (on average about 14% overprediction in strain range 9 to 18). However, as shown in Fig. 4, the model predicts the general occurrence of a slowing down of grain refinement for alloys with alloys with 99.5 to ~90% Al quite well. In the model the slowing down of grain size refinement is in essence due to the proportionality relations $\varepsilon \propto \rho \propto S_v \propto 1/d$. The data in our database is for alloys with alloys with 99.5 to ~90% Al, and it is thought that dynamic recovery is suppressed by the solute in the matrix [114].

In the model (i.e. in the absence of annihilation of dislocations within the grains) a practical limit to grain refinement is encountered when the sample fails (cracks), which effectively can be understood as the extremely high density of microscale defects (dislocations and grain boundaries) and their microscale stress fields causing a macroscale defect by initiating cracks. This type of failure can be delayed by subjecting the deforming material to compressive stresses; this is especially used in HPT, where the sample is contained and compressed, and in ECAP with back pressure. As a guide we can make an estimate of grain size refinement achievable in Al alloys. For this we take values of parameters that would be maximum achievable: $K_A=930\text{MPa}$ (a solution treated Al-10Mg-0.25Zr alloy with dispersoid size $r=10\text{nm}$), $\varepsilon=25$. This provides $d=20\text{nm}$. However, such alloys are known to be very brittle and it may be very doubtful if $\varepsilon=25$ can be reached even with extensive compressive forces. A more reasonable choice of composition would be Al-5Mg-0.25Zr which would give $d=30\text{nm}$. According to the present model further grain refinement is not possible in Al based alloys.

7. Summary

The work hardening behaviours at strains up to 0.05 and the grain refinement during severe plastic deformation up to a strain of 16 at room temperature of a wide range of alloys was investigated. A model was presented for the grain refinement and the model for hardening in the parabolic regime was expanded.

The work hardening analysis showed:

It is confirmed that the work hardening factor depends on the dislocation free path related to the presence of non shearable particles. These particles give rise to dislocation multiplication in the form of generation of geometrically necessary dislocations.

It is found that work hardening factor depends strongly on Mg content. It show that the hardening effect can be quantitatively related to an effective dislocation free path related to the presence repulsive forces of Mg-Mg nearest neighbour interactions, which require the generation of additional dislocations. The work hardening can be understood using the concept of these chemically necessary dislocations.

The grain refinement model showed:

The model for grain development considers the dislocations generated, ρ_{gen} , including the geometrically necessary dislocations and the chemically necessary dislocations and considers that they distribute to create cell walls with effective volume averaged dislocation densities, ρ_{cw} , and move to existing cell walls/grain boundaries and cause an increase in the grain boundary misorientation.

The average grain boundary misorientation, which is a model parameter, was determined through analysis of grain boundary misorientation density functions obtained for several alloys that were processed by ECAP. There are no fittable parameters.

The model predicts grain size to an accuracy of about 22%.

Analysis shows that the model correctly predicts the considerable influence of Mg content and content of non-shearable particles on the grain refinement.

Acknowledgements

We gratefully acknowledge the following. Dr. Z. Zhu and Dr. N. Kamp for tensile tests on 5xxx and 7xxx alloys. Prof. T.G. Langdon for valuable discussions on SPD and grain refinement. Dr C. Xu for valuable discussions on ECAP. Dr. S.C. Wang for assistance with SEM, EBSD and TEM. Mr. N. Finecountry for SEM on HPT processed Al-1050 and Al-3Mg-0.4Mn. Alcan International, QinetiQ and Prof. H. Roven for providing selected alloys

Appendix: Determination of volume fraction and sizes of non-shearable particles

If l_g is smaller or comparable to l_{ch} , both K_A and grain refinement is influenced by content of non-shearable intermetallic phases. The volume fractions of these intermetallic phases can be estimated from thermodynamic data (phase diagrams and thermodynamic prediction software). This has been applied throughout this work, with the exception of the Al-5Fe alloys, where the high density of Fe containing intermetallics was determined from TEM data in [36]; and for the Al-1050 alloy for which f was estimated on the basis of a linear dependency on (Fe+Si) content (in wt%) from data [115]. (Analysis has shown that the intermetallic particles in these alloys are predominantly β -AlFeSi (Al_5FeSi) and α -AlFeSi (Al_8Fe_2Si) [115]). This provided $f = 0.76$ and 1.01 vol% for the Al-1050 alloys used for ECAP and HPT processing, respectively. Particle sizes were determined from TEM and SEM work. Both TEM data on Al-1100 from [77] and our own SEM experiments on HPT processed (2 turns, $\epsilon \sim 4$) Al-1050 show $r = 50$ nm. Hence for Al-1050, Al-1100, Al-97% and Al-3004, which are all thought to contain predominantly β -AlFeSi (Al_5FeSi) and α -AlFeSi (Al_8Fe_2Si), we take r as 50 nm. For the Al-4Cu alloy r was determined from TEM work in [76] as 5 nm. For the Al-7Si and Al-0.5Si alloy r was taken from TEM data in [30] as 13 nm. For the Zr containing alloys the size of Al_3Zr dispersoids was taken as 20nm (in the alloys considered here, Al_3Zr dispersoids do not have a significant influence on K_A because the volume fractions are very low).

References

- 1 Segal VM, Reznikov VI, Drobyshevskiy AE, Kopylov VI. *Russian Metall* 1981;1:99.
- 2 Segal VM. *Mater Sci Eng A* 1995;97:57.
- 3 Valiev RZ, Langdon TG. *Prog Mater Sci* 2006;51:881.
- 4 Nakashima K, Horita Z, Nemoto M, Langdon TG. *Mater Sci Eng* 2000;A281:82.
- 5 Zhilyaev AP, Langdon TG. *Prog Mater Sci* 2008;53:893.
- 6 Bridgman PW. *Studies in large plastic flow and fracture*. McGraw-Hill, New York, NY, USA; 1952.
- 7 Horita Z, Langdon TG. *Mater Sci Eng A* 2005;410-411:422.
- 8 Baretzky B, Baró MD, Grabovetskaya GP, Gubicza J, Ivanov MB, Kolobov YuR, Langdon TG, Lendvai J, Lipnitskii AG, Mazilkin AA, Nazarov AA, Nogués J, Ovidko IA, Protasova SG, Raab GI, Révész Á, Skiba NV, Sort J, Starink MJ, Straumal BB, Suriñach S, Ungár T, Zhilyaev AP. *Rev Adv Mater Sci* 2005;9:45.
- 9 Valiev RZ, Salimonenko DA, Tsenev NK, Berbon PB, Langdon TG. *Scripta Mater* 1997;37:1945.
- 10 Zhu YT, Langdon TG. *Mater Sci Eng A* 2005;409:242.
- 11 Wu XL, Ma E, Zhu YT. *J Mater Sci* 2007;42:1427.
- 12 Liu MP, Roven HJ, Murashkin M, Valiev RZ. *Mater Sci Eng A* 2009;503:122.
- 13 Liao XZ, Zhao YH, Srinivasan SG, Zhu YT, Valiev RZ, Gunderov DV. *Appl Phys Lett* 2004;84:592.
- 14 Liu MP, Roven HJ, Yu Y, Werenskiold JC. *Mater Sci Eng A* 2008;483-484:59.
- 15 Chen MW, Ma E, Hemker KJ, Sheng HW, Wang YM, Cheng XM. *Science* 2003;300:1275.
- 16 Valiev RZ, Ivanisenko YV, Rauch EF, Baudalet B. *Acta Mater* 1996;44:4705.
- 17 Sevillano JG, Aernoudt E. *Mater Sci Eng A* 1987;86:35.
- 18 Argon AS, Haasen P. *Acta Metall Mater* 1993;41:3289.
- 19 Zehetbauer M, Seumer V. *Acta Metall Mater* 1993;41:577.
- 20 Rollett AD, Kocks UF. *Solid State Phenomena* 1994;35-36:1.
21. Ashby MF. In: Kelly K, Nicholson RB, editors. *Strengthening Methods in Crystals*, Elsevier, Amsterdam, The Netherlands, 1971. p.137.
- 22 Valiev RZ. *Nat Mater* 2004;3:511.
- 23 Valiev RZ, Islamgaliev RK, Alexandrov IV. *Prog Mater Sci* 2000;45:103.
- 24 Chang CP, Sun PL, Kao PW. *Acta mater.* 2000;48:3377
- 25 Langdon TG. *Mater Sci Eng A* 2007;462:3.
- 26 Xu C, Furukawa M, Horita Z, Langdon TG. *Mater Sci Eng A* 2005;398:66.
- 27 Hughes DA. *Mater Sci Eng A* 2001;319:46.
- 28 Jazaeri H, F.J Humphreys. *Acta Mater* 2004;52:3239 .
- 29 Q. Liu, X. Huang, D.J. Lloyd and N. Hansen. *Acta Mater.* 2002;50:3789.
- 30 Munoz Morris MA, Gutierrez-Urrutia I, Morris DG. *Mater Sci Eng A* 2008;493:141.
- 31 Beyerlein IJ, Lebensohn RA, Tome CN. *Mater Sci Eng A* 2003;345:122.
- 32 Signorelli JW, Turner PA, Sordi V, Ferrante M, Vieira EA, Bolmaro RE. *Scripta Mater* 2006;55:1099.
- 33 Wang SC, Starink MJ, Gao N, Xu C, Langdon TG. *Rev Adv Mater Sci* 2005;10:249.
- 34 Xu C, Dixon W, Furukawa M, Horita Z, Langdon TG. *Mater Lett* 2003;57:3588.
- 35 Gao N, Starink MJ, Furukawa M, Horita Z, Xu C, Langdon TG. *Mater Sci Eng A* 2005;410-411:303.
- 36 Stolyarov VV, Lapovok R, Brodova IG, Thomson PF. *Mater Sci Eng A* 2003;357:159.
37. Underwood E. *Quantitative Stereology*, Addison-Wesley, Cambridge Massachusetts, 1970.
- 38 Zhu Z, Starink MJ. *Mater Sci Eng A* 2008;489:138.
- 39 Kamp N, Gao N, Starink MJ, Sinclair I. *Int J Fatigue* 2007;29:869.
- 40 Gao N, Starink MJ, Davin L, Cerezo A, Wang SC, Gregson PJ. *Mater Sci Tech* 2005;21:1010.

-
- 41 Estrin Y, Toth LS, Molinari A, Brechet Y. *Acta Mater* 1998;46:5509.
 - 42 Baik SC, Estrin Y, Kim HS, Hellmig RJ. *Mater Sci Eng A* 2003;351:86.
 - 43 Toth L, Molinari A, Estrin Y. *J Eng Mater Tech* 2002;124:71.
 - 44 Field DP, Weiland H. In: Schwartz AJ, Kumar M, Adams BL, editors. *Electron Backscatter Diffraction in Materials Science*, Kluwer Acad, New York, 2000. p. 199.
 - 45 Iwahashi Y, Horita Z, Nemoto M, Langdon TG. *Acta Mater* 1998;46:3317.
 - 46 Reihanian M, Ebrahimi R, Moshksar MM, Terada D, Tsuji N. *Mater Char* 2008;59:1312.
 - 47 Iwahashi Y, Wang J, Horita Z, Nemoto M, Langdon TG. *Scripta Mater* 1996;35:143.
 48. Gubicza J, Chinh NQ, Horita Z, Langdon TG. *Mater Sci Eng A* 2004;387-389:55.
 - 49 Kocks UF. *Phil Mag* 1966;13:541.
 - 50 Mecking H, Kocks UF. *Acta Metall Mater* 1981;29:1865.
 - 51 Kocks UF, Mecking H. *Prog Mater Sci* 2003;48:171.
 - 52 Ashby MF. *Phil Mag* 1970;21:399.
 - 53 Wang SC, Zhu Z, Starink MJ. *J Microscopy* 2005;217:174.
 - 54 Estrin Y, Mecking H. *Acta Metall Mater* 1984;32:57.
 55. Kamp N, Sinclair I, Starink MJ. *Metall Mater Trans A* 2002; 33:1125.
 - 56 Kenji N, Shumpei K, Koki N, Yoshikazu S, Takehiko M. *Research Reports of the Faculty of Engineering, Kagoshima University*, 1999.
 57. Zolotarevsky NY, Solonin AN, Churyumov AY, Zolotarevsky VS. *Mater Sci Eng A* 2009;502:111.
 58. Waldron GWJ. *Acta Metall Mater* 1965;13:897.
 59. Hughes DA. *Acta Metall Mater* 1993;41:1421.
 60. Brown LM, Ham RK, in “*Strengthening Methods in Crystals*”, ed. A. Kelly and R.B. Nicholson, Elsevier, Amsterdam, The Netherlands, 1971, p. 9.
 61. Starink MJ, Wang P, Sinclair I, Gregson PJ. *Acta Mater* 1999;47:3855.
 62. Starink MJ, Wang SC. *Acta Mater* 2009;57:2376.
 63. Zhu Z, Starink MJ. *Mater Sci Eng A* 2008;488:125.
 64. Zhu Z, Starink MJ. In: Howe JM, Laughlin DE, Lee JK, Srolovitz DJ, Dahmen U, editors. *Solid-Solid Phase Transformations in Inorganic Materials 2005*, TMS, Warrendale, PA, USA, 2005. p. 383.
 - 65 Starink MJ, Wang SC. *Acta Mater* 2003;51:5131.
 - 66 Rometsch PA, Wang SC, Harriss A, Gregson PJ, Starink MJ. *Mater Sci Forum* 2002;396-402:655.
 - 67 Nes E, Marthinsen K. *Mater Sci Eng A* 2002;322:176.
 - 68 Bowen JR, Prangnell PB, Jensen DJ, Hansen N. *Mater Sci Eng A* 2004;387-389:235.
 - 69 Hansen N. *Scripta Mater* 2004;51:801.
 - 70 Friel JJ. *Practical Guide to Image Analysis*, ASM International, 2000.
 - 71 Thorvaldsen A. *Acta Mater* 1997;45:587.
 - 72 J.K. Mackenzie, *Biometrika* 45 (1958) 229 (<http://biomet.oxfordjournals.org/cgi/reprint/45/1-2/229>)
 - 73 Morris DG, Munoz-Morris MA. *Acta Mater* 2002;50:4047.
 - 74 Hasegawa H, Komura S, Utsunomiya A, Horita Z, Furukawa M, Nemoto M, Langdon TG. *Mater Sci Eng A* 1999;265:188.
 - 75 Lee S, Utsunomiya A, Akamatsu H, Neishi K, Furukawa M, Horita Z, Langdon TG. *Acta Mater* 2002;50:553.
 - 76 Prados EF, Sordi VL, Ferrante M. *Mater Research* 2008;11:199.
 - 77 Horita Z, Fujinami T, Nemoto M, Langdon TG. *Metall Mater Trans A* 2000;31:691.
 - 78 Dobatkin SV, Zakharov VV, Vinogradov AY, Kitagawa K, Krasil'nikov NA, Rostova TD, Bastarash EN. *Russian Metallurgy (Metally)* 2006;6:533.
 - 79 Starink MJ, Qiao XG, Zhang J, Gao N. *Database of grain sizes of HPT processed Al alloys*, www.eprints.soton.ac.uk/66237/

-
- 80 Apps PJ, Berta M, Prangnell PB. *Acta Mater* 2005;523:499.
- 81 Furukawa M, Iwahashi Y, Horita Z, Nemoto M, Tsenev NK, Valiev RZ, Langdon TG. *Acta Mater* 1997;45:4751.
- 82 Furukawa M, Berbon PB, Horita Z, Nemoto M, Tsenev NK, Valiev RZ, Langdon TG. *Metall Mater Trans A* 1998;29:169.
- 83 Hansen N, Jensen DJ. *Phil Trans* 1999;357:1447.
- 84 Kratochvil J, Kruzik M, Sedlacek R. *Acta Mater* 2009;57:739.
- 85 Zhao YH, Liao XZ, Jin Z, Valiev RZ, Zhu YT. *Acta Mater* 2004;52:4589.
- 86 Chowdhury SG, Mondal A, Gubicza J, Krallics G, Fodor A. *Mater Sci Eng A* 2008;490:335.
- 87 Gubicza J, Chinh NQ, Krallics Gy, Schiller I, Ungar T. *Current Applied Physics* 2006;6:194.
- 88 Iwahashi Y, Horita Z, Nemoto M, Langdon TG, *Metall Mater Trans A* 1998;29:2503.
- 89 Qiao X, Starink MJ, Gao N, *Mater Sci Eng A* 2009;513-514:52.
- 90 Hansen N, Huang X, Hughes DA. In: *Ultrafine Grained Materials II (2002 TMS Annual Meeting)*, Seattle, WA, USA, 2002. p. 3.
- 91 Godfrey A, Hughes DA. *Scripta Mater* 2004;51:831.
- 92 Sitdikov O, Sakai T, Miura H, Hama C. *Mater Sci Eng A* 2009;516:180.
- 93 Mazurina I, Sakai T, Miura H, Sitdikov O, Kaibyshev R. *Mater Sci Eng A* 2008;486:662.
- 94 Sitdikov O, Sakai T, Avtokratova E, Kaibyshev R, Tsuzaki K, Watanabe Y. *Acta Mater* 2008;56:821.
- 95 Islamgaliev RK, Yunusova NF, Sabirov IN, Sergueeva AV, Valiev RZ. *Mater Sci Eng A* 2001;319-321:877.
- 96 Enikeev NA, Kim HS, Alexandrov IV. *Mater Sci Eng A* 2007;460-461:619.
- 97 Starink MJ, Zahra AM. *Phil Mag A* 1997;76:701.
- 98 Horita Z, Smith DJ, Furukawa M, Nemoto M, Valiev RZ, Langdon TG. *J Mater Res* 1996;11:1880.
- 99 Ito Y, Horita Z. *Mater Sci Eng A* 2009;503:32.
- 100 Saxl I, Kalousova A, Ilucova L, Sklenicka V. *Mater Char*, in press, 2009.
- 101 Bui QH, Dirras GF, Hocini A, Ramtani S, Abdul-latif A, Gubicza J, Chauveau T, Fogarassy Z, *Mater Sci Forum* 2008;584-586:579.
- 102 Chang SY, Lee KS, Choi SH, Shin DH. *J Alloys Compounds* 2003;354:216.
- 103 Billard S, Fondere JP, Bacroix B, Dirras GF. *Acta Mater* 2006;54:411.
- 104 El-Danaf EA. *Mater Sci Eng A* 2008;487:189.
- 105 Saravanan M, Pillai RM, Pai BC, Brahmakumar M, Ravi KR. *Bull Mater Sci* 2006;29:679.
- 106 Dingley DJ. In: Schwartz AJ, Kumar M, Adams BL, editors. *Electron Backscatter Diffraction in Materials Science*, Kluwer Acad, New York, 2000, p. 1.
- 107 Prangnell PB, Huang Y, Berta M Apps PJ, In: P.B. Prangnell and P.S. Bate, Editors, *Proc of the intern. symp. on fundamentals of deformation and annealing*, TransTech, Zurich (2007), p. 160.
- 108 Pirgazi H, Akbarzadeh A, Petrov R, Kestens L, *Mater Sci Eng A* 2008; 497:132.
- 109 Hebesberger T, Stüwe HP, Vorhauer A, Wetscher F, Pippan R, *Acta Mater* 2005;53:393.
- 110 Kawasaki M, Horita Z, Langdon TG, *Mater Sci Eng A*, in press, doi: 10.1016/j.msea.2009.06.032.
- 111 Mohamed FA, *Acta Mater* 2003;51:4107.
- 112 Qu S, An XH, Yang HJ, Huang CX, Yang G, Zang QS, Wang ZG, Wu SD, Zhang ZF, *Acta Mater* 2009; 57:1586.
- 113 Zhao YH, Liao XZ, Zhu YT, Horita Z, Langdon TG, *Mater Sci Eng A* 2005; 410 188.
- 114 Hong SI, Gray GT, Lewandowski JJ, *Acta Metall Mater*1993; 41:2337.
- 115 Stephen G, MSc thesis, McMaster University, Canada, 1994.